

Y.E. ROMANYUK^{1,✉}
D. EHRENTAUT¹
M. POLLNAU¹
S. GARCÍA-REVILLA²
R. VALIENTE²

Low-temperature flux growth of sulfates, molybdates, and tungstates of Ca, Sr, and Ba and investigation of doping with Mn⁶⁺

¹ Advanced Photonics Laboratory, Institute of Imaging and Applied Optics,
Swiss Federal Institute of Technology, 1015 Lausanne, Switzerland

² Dpto. Física Aplicada, Facultad de Ciencias, Universidad de Cantabria, Avda. de Los Castros s/n,
39005 Santander, Spain

Received: 28 August 2003/Accepted: 15 December 2003
Published online: 23 March 2004 • © Springer-Verlag 2004

ABSTRACT The growth of undoped and Mn⁶⁺-doped molybdates and tungstates of alkali-earth metals and BaSO₄ has been investigated. Single crystals were grown by the flux method within the temperature range of 600–475 °C, using the ternary NaCl–KCl–CsCl solvent. Sizes of undoped crystals increase within the series tungstates < molybdates < sulfate and, depending on the cation, within the series Ca²⁺ ≈ Sr²⁺ < Ba²⁺. The Mn⁶⁺ ion tends to be reduced to Mn⁵⁺/Mn⁴⁺ with time in the chloride solution, but can be partly stabilized by the addition of alkali-metal carbonates or hydroxides. The incorporation of Mn⁶⁺ is governed by the coordination of the MnO₄^{2–} tetrahedron in the crystal. No significant doping was found for Ca and Sr compounds and only small amounts of Mn⁶⁺ were incorporated into BaMoO₄ and BaWO₄. Crystals with orthorhombic space group *Pnma* such as BaSO₄ exhibit significantly higher doping levels. The Mn⁶⁺ distribution in each crystal varies due to manganese reduction with growth time. Temperature-, time-, and concentration-dependent spectroscopy of BaSO₄:Mn⁶⁺ was performed.

PACS 61.72.Ww; 81.05.Je; 81.10.Dn

1 Introduction

AXO₄ single crystals are promising host materials for the incorporation of optically active hexavalent ions in tetrahedral oxo-coordination. A large variety of methods have been used to grow AXO₄ single crystals, with A = Ca, Sr, Ba and X = Mo, W, including the hydrothermal, Verneuil, laser-heated pedestal, Bridgman–Stockbarger, and Czochralski techniques [1–5]. In contrast, growth from the melt fails in the case of another crystal with tetrahedral oxo-coordination, BaSO₄, owing to a phase transition at 1090 °C [6] and thermal decomposition at 1590 °C below the melting point.

Small but rather high-quality crystals of all these compounds can be prepared by crystallization from alkali-metal chloride solutions [7–11]. Such a flux growth is possible at temperatures much lower than the melting points of

the molybdates, tungstates, and sulfates, thus offering specific advantages over growth from the melts. First, the flux growth is slow and the growing crystal is not exposed to a high temperature gradient, which could be detrimental to producing crack-free crystals. Second, a low growth temperature is essential if, for example, the compound exhibits a phase transition below its melting point, as is the case for BaSO₄. On the other hand, problems related to choosing a suitable solvent, optimizing the solute concentration, and minimizing the imperfections of flux-grown crystals must be solved when employing the growth from solutions.

A low growth temperature is also required if the desired oxidation state of a doping ion is not stable at the melting-point temperature of the host and, thus, the ion cannot be incorporated in this oxidation state when growing from the melt. The Mn⁶⁺ ion is a promising activator ion for future tunable lasers [12, 13] and broadband fluorescent light sources [14] for applications in interferometry [15, 16]. It can be incorporated into a number of hosts with tetrahedral oxo-coordination, such as sulfates, selenates, chromates, and molybdates [17], at the tetrahedral X⁶⁺ sites where no charge compensation is required. However, Mn⁶⁺ tends to be reduced to Mn⁵⁺ at temperatures above ~ 600 °C [18]. Therefore, satisfactory results on the incorporation of manganese in its hexavalent oxidation state have been obtained only with low-temperature flux-growth techniques [13, 19].

In this study, we investigate the flux growth of molybdates and tungstates of Ca, Sr, and Ba as well as BaSO₄ using the ternary NaCl–KCl–CsCl solvent at temperatures well below 600 °C. The concentration series and the solubility of AXO₄ in the chosen chloride solvent are investigated in order to determine the most suitable growth conditions. BaSO₄:Mn⁶⁺ has so far shown the highest luminescence quantum efficiency at room temperature [20]. Tungstates and molybdates of Ca, Sr, and Ba could be interesting host materials for real-world applications, because they possess higher thermal conductivity and mechanical stability than BaSO₄. A systematic investigation of the incorporation of Mn⁶⁺ ions into the above AXO₄ crystals is performed. Physical and chemical factors influencing the incorporation of the Mn⁶⁺ ion into the host are discussed. The basic spectroscopic properties of Mn⁶⁺-doped

✉ Fax: +41-21/693-3701, E-mail: yaroslav.romanyuk@epfl.ch

BaSO₄ are investigated with respect to the Mn⁶⁺ concentration. This host possesses the highest potential for the efficient incorporation of Mn⁶⁺ as an active ion.

2 Flux growth of AXO₄

2.1 Selection of the solvent

The continuous-cooling method has been widely used for the flux growth of undoped AXO₄ crystals from pure LiCl and alkali-earth-metal chloride solvents [7], as well as from NaCl and KCl solvents [8–10]. The lowest growth temperature is limited by the solidification point of the solvent, which is 610, 801, 771, and 646 °C for LiCl, NaCl, KCl, and CsCl, respectively [21]. Therefore, we used the ternary NaCl–KCl–CsCl solvent [12, 11]. The solvent composition corresponds to the eutectic point of the ternary system [22] with a eutectic temperature of 482 °C, which is significantly lower than the melting points of the individual chlorides contained in the composition. In this way, we could apply lower growth temperatures and reduce undesirable reactions in the flux, such as the reduction of Mn⁶⁺ to Mn⁵⁺.

The ternary solvent possesses low viscosity and volatility. The total mass loss by evaporation was less than 1 wt. % in all the experiments. The Na, K, and Cs chlorides are non-toxic and available in high purities, which is necessary to minimize impurity incorporation into the crystal. Finally, the AXO₄ phase is the only stable solid phase in the solution. Since all the grown AXO₄ crystals are insoluble in water, they can be easily separated from the flux by dissolving the flux in water.

2.2 Experimental procedure

Chlorides with purities better than 99.99 wt. % were dried at 200 °C for 20 h and the eutectic composition of 30.4, 24.4, and 45.2 mol% of NaCl, KCl, and CsCl, respectively, was thoroughly mixed to be used as a solvent. The solute was introduced in two ways: either as a stoichiometric mixture of the AO oxides with XO₃ or as AXO₄ powder. Total solution charges of 14 g with AXO₄ contents up to 4 mol% were filled into alumina crucibles and placed without lids in a resistance-heated furnace. The solutions were heated under ambient atmosphere at a rate of 120 K h^{−1} to 600 °C, held at this temperature for 6 h, and then cooled at a rate of 1.8 K h^{−1} down to 475 °C. Afterwards, the furnace was cooled to room temperature at a higher cooling rate. Crystals were separated by dissolving the solidified flux in water. The amounts of AXO₄ residues varied from 80 to 90% with respect to the initial solute charges.

2.3 Solubility

The flux growth was carried out by the slow-cooling method with spontaneous nucleation, which normally yields a large number of small crystals. In order to estimate the optimal growth conditions and produce a small number of large-size crystals of satisfying quality, the dependence of crystal size on solute concentration (C_{solute}) was investigated for all seven compounds. For each flux experiment, the 10 largest crystals were selected, their sizes measured, and the

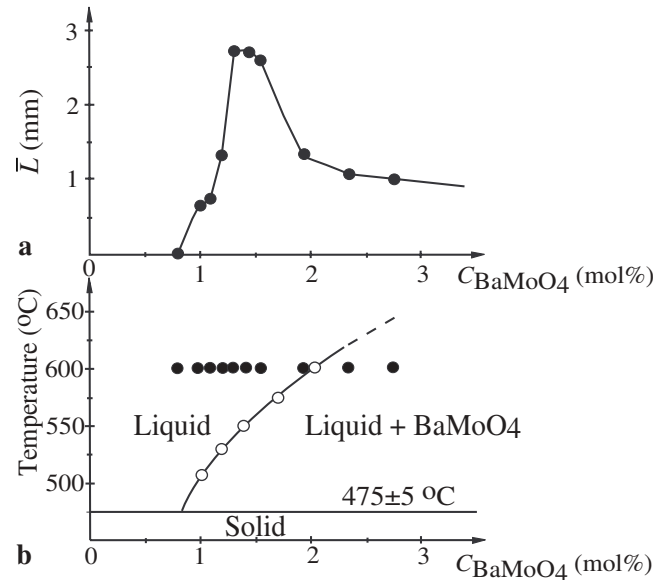


FIGURE 1 **a** Dependence of \bar{L} on C_{BaMoO_4} . **b** The solubility of BaMoO₄ in the ternary NaCl–KCl–CsCl solvent measured in the temperature interval 500–600 °C. The solubility curve (open circles) is given together with the starting solution compositions (filled circles) used for the flux growth of BaMoO₄

average size \bar{L} was calculated. The derived dependence of \bar{L} on C_{solute} was similar for all the compounds.

Here, BaMoO₄ is chosen as an example, because the possibility of incorporating Mn⁶⁺ into BaMoO₄ was previously demonstrated [17]. The curve is characterized by the presence of a maximum (see Fig. 1a). In order to explain this trend, we investigated the solubility of each compound in the chloride flux by the dissolution–extraction method. As-grown crystals (0.2–2 mm in size) were placed onto a slowly rotating alumina holder and immersed into the liquid solvent being kept at constant temperature. After saturation for 24 h, the remaining undissolved crystals were withdrawn and the mass change determined. The solubility curves within the temperature range 500–600 °C were constructed for all seven compounds (see Fig. 1b for the result on BaMoO₄).

We treat our solution as a pseudo-binary system with the BaMoO₄ phase as one component and the chloride solvent as the other. The eutectic temperature of the pseudo-binary system was found to be 475 ± 5 °C using differential-thermal analysis (DTA). An extrapolation of the liquidus (solubility) curve resulted in the eutectic coordinate of 0.8 mol% BaMoO₄.

The size and quality of the grown crystals depend on whether the growth starts from an unsaturated or saturated solution. If the initial composition at 600 °C is located above the liquidus curve, the solution is unsaturated. Solutions containing less than 0.8 mol% BaMoO₄ are unsaturated even at the solidification point. In this case, no crystals but fine-grade powder was observed. Solutions with BaMoO₄ content from 0.8 to 2.0 mol% cross the liquidus curve when cooling from 600 °C to the solidification point, the solution becomes supersaturated, spontaneous nucleation occurs, and a small number of large crystals is obtained. \bar{L} increases rapidly and forms a maximum at the concentration of 1.3 mol%. Above 1.3 mol%, \bar{L} decreases again, although the initial composi-

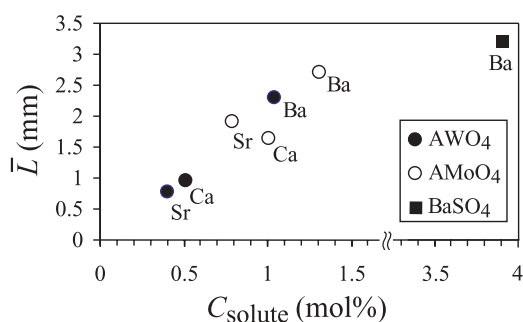


FIGURE 2 Maximum \bar{L} versus C_{solute} for molybdates and tungstates of Ca, Sr, and Ba as well as for BaSO₄

tion is still above the liquidus curve. This small misfit is due to the fact that the crystallization/dissolution process occurs in a certain temperature interval (Ostwald–Miers region) around the liquidus curve. If the initial composition contains ≥ 2 mol% BaMoO₄, it is located below the liquidus curve already at 600 °C, i.e. the growth starts from the saturated solution with a certain amount of undissolved BaMoO₄. The large number of solid solute particles serve as nucleation centers, resulting in a large number of small crystals, as can be seen in Fig. 1b.

Figure 2 displays the location of the maximum \bar{L} with respect to C_{solute} for all seven compounds. The sizes of the crystals increase in the series tungstates < molybdates < sulfate and, depending on the cation, in the series Ca \approx Sr < Ba. The solubility changes in the same way, i.e. the highest solubility in the chloride flux was observed for BaSO₄ (1.90 mol% or 4.0 g in 100 g of flux at 550 °C).

The solubility of alkali-earth-metal tungstates in different chloride solutions correlates with the thermodynamical stability of each solution [23], which can be expressed numerically by the excess free energy of mixing, $\Delta G^E = \Phi(1/r_A - 1/r_N)$. As the metal cation radii r_A increase in the series Ca²⁺ < Sr²⁺ < Ba²⁺, ΔG^E decreases for a given solvent cation radius r_N ; Ba-containing solutions are, therefore, the most thermodynamically stable solutions, exhibit the highest solubility, and, consequently, produce the largest crystals. For the same cation, tungstate crystals are smaller than molybdate and sulfate crystals in our experiments. Since the chemical nature and ionic radii of Mo⁶⁺ and W⁶⁺ (0.55 and 0.56 Å, respectively [24]) are similar, the only discriminating factor between MoO₄²⁻ and WO₄²⁻ are their molar masses. The WO₄²⁻ complex ion is heavier than the MoO₄²⁻ and SO₄²⁻ complex ions. Therefore, it exhibits the lowest diffusion coefficient, resulting in the smallest crystals.

2.4 Crystal characterization

The dimensions and morphology of the grown crystals were investigated by optical microscopy. The largest crystals were observed for BaSO₄. They were prismatic, elongated in the [100] direction, and up to 4-mm long. In the case of Ca and Sr molybdates and tungstates, many highly transparent crystals were grown. Low growth rates of 5–10 $\mu\text{m h}^{-1}$ yielded small but well-developed crystals of high optical quality. Crystal polyhedra of CaWO₄ with {112}, {101}, {211}, and {2 $\bar{1}$ 3} faces were found. Higher growth rates of 50 $\mu\text{m h}^{-1}$ were observed for BaMoO₄, resulting in tetragonal bipyramidal crystals. X-ray diffraction of the oriented BaMoO₄ crystals shows that the tetragonal bipyramids are elongated in the *c*-axis direction and bounded by {101} faces. Large crystals were only partly transparent because of cracks and inclusions. Re-entrant angles were strongly developed for BaWO₄, which crystallized in the form of a tetrahedral pyramid.

The phase purity of the grown crystals was confirmed by X-ray powder diffraction (XRD) using an X'Pert Philips powder diffractometer with Cu *K*_α radiation. Si was used as the internal standard. Lattice constants were calculated from Rietveld refinement analysis using the XND software package [25]. The investigated tungstates and molybdates possess the scheelite structure, space group *I*4₁/*a*, with four A²⁺ ions and four XO₄²⁻ tetrahedra per unit cell. The estimated lattice constants listed in Table 1 agree well with or are slightly larger than those reported in the literature.

3 Doping with Mn⁶⁺

According to the results of our preliminary flux experiments, we employed solute concentrations of 0.60, 0.55, and 1.15 mol% of CaWO₄, SrWO₄, and BaWO₄, respectively, 0.8, 1.15, and 1.55 mol% of CaMoO₄, SrMoO₄, and BaMoO₄, respectively, and 4 mol% of BaSO₄ in order to investigate the incorporation of Mn⁶⁺ as an optically active dopant into the above crystals. K₂MnO₄ was used as the source of Mn⁶⁺ ions in concentrations of 0.2–15 mol% with respect to the solute. Generally, the challenge of manganese doping consists of two parts: (i) stabilization of manganese in its hexavalent oxidation state in the solution during the entire growth period and (ii) incorporation of Mn⁶⁺ into the different host lattices. Once a sufficiently high amount of Mn⁶⁺ can be incorporated into a specific host lattice, determination of the Mn⁶⁺ concentration and quantitative spectroscopy can be performed in this host.

Compound	Lattice constants (Å) [26]		Lattice constants (Å) [our data]		Melting point (°C) [22]	Density calculated (g/cm ³)
	<i>a</i>	<i>c</i>	<i>a</i>	<i>c</i>		
CaMoO ₄	5.226	11.430	5.22705(4)	11.4351(1)	1445	4.25
SrMoO ₄	5.3944	12.020	5.39648(4)	12.0263(1)	1457	4.70
BaMoO ₄	5.5802	12.821	5.58245(5)	12.8212(2)	1459	4.95
CaWO ₄	5.243	11.376	5.24426(7)	11.3767(2)	1580	6.12
SrWO ₄	5.4168	11.951	5.41865(3)	11.9541(1)	1535	6.35
BaWO ₄	5.6134	12.720	5.61560(6)	12.7212(2)	1475	6.38

TABLE 1 Crystallographic and physical parameters of the AXO₄ compounds (space group *I*4₁/*a*)

3.1 Stability of the Mn^{6+} ion in the chloride solution

The Mn^{6+} ion tends to be reduced to lower oxidation states in the solution even at temperatures below 600 °C, and varying amounts of dark-brown MnO_2 were always found at the bottom of the crucible after the growth process, independently of whether the solute AXO_4 was added as AXO_4 powder or was formed in the solution by a chemical reaction of AO and XO_3 .

We investigated the time dependence of the Mn^{6+} concentration in the chloride solution at a constant temperature of 550 °C by observing the intensity of the green color that is characteristic of manganese in its hexavalent oxidation state (Fig. 3). Compared to a reference solution containing only the chloride solvent and K_2MnO_4 , the presence of an AXO_4 solute accelerates the reduction of manganese. The reduction speed increases within the series $\text{Ba} < \text{Sr} < \text{Ca}$. No green color was observed in CaXO_4 -containing solutions immediately after melting the charge, whereas the reference solution exhibited a rich green color during 32 h. The addition of a small amount of alkali carbonate or hydroxide can stabilize the Mn^{6+} ion [27]. Introduction of K_2CO_3 or NaOH into our solutions indeed prolonged the stability of Mn^{6+} , and its availability during the entire growth period was guaranteed for Sr- and Ba-containing compounds. Figure 3 illustrates the temporal degradation of the green color of solutions containing 6 mg K_2MnO_4 without and with addition of 50 mg K_2CO_3 .

Evidently, the presence of the oxygen-containing additives or oxygen atmosphere [28] plays a dominant role in the stabilization of hexavalent manganese. The Mn^{6+} ion is known only as the manganate complex MnO_4^{2-} [29]. Certain solution components may react with the oxygen ions in the manganate complex, which leads to a decomposition of this

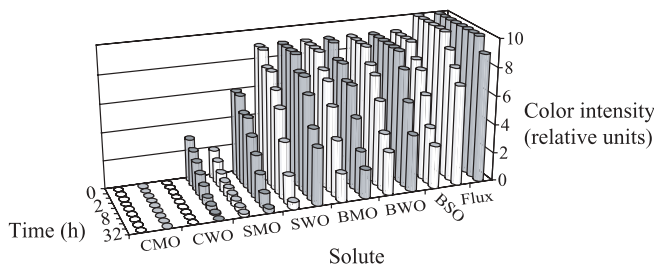


FIGURE 3 Time-dependent degradation of the intensity of green color, as a consequence of the reduction of Mn^{6+} ions, for the solutions without (white columns) and with the addition of K_2CO_3 (shaded columns). Abbreviations: AXO = AXO_4 , Flux = solvent only. All solutions contained 1 mol% K_2MnO_4 with respect to the solute

complex and, consequently, to the reduction of Mn^{6+} . Since the stability of Mn^{6+} decreases significantly from Ba- to Ca-containing solutions, it is likely that the solute cation A^{2+} binds an oxygen ion from the manganate complex. According to the Lewis theory, we can consider the solute cation A^{2+} as an acid (electrophile) and the MnO_4^{2-} complex ion as a weak base (nucleophile) [29]. Ca^{2+} possesses the strongest electrophile properties and reacts more likely with the MnO_4^{2-} complex ion, resulting in the lowest stability of MnO_4^{2-} in the chloride solutions with Ca compounds. However, the reduction process can be more complicated and involve further reactions, e.g. an intrinsic decomposition of K_2MnO_4 [18].

3.2 Incorporation of the Mn^{6+} ion into AXO_4 crystalline lattices

Our grown Mn^{6+} -doped crystals showed the same habits and proportions as their undoped counterparts. BaSO_4 crystals doped with Mn^{6+} were pink, BaMoO_4 and BaWO_4 crystals were light green, whereas Ca and Sr compounds were colorless, independently of the initial K_2MnO_4 concentration. Electron-probe microanalysis (EPMA) of BaSO_4 crystals showed that the actual manganese concentration varied from 240 to 2100 ppm depending on the initial K_2MnO_4 concentration. For molybdates and tungstates, the manganese concentration was less than 60 ppm, i.e. below the detection limit of EPMA (Table 2).

When considering substitution of the X^{6+} by the Mn^{6+} ion in the AXO_4 host, the most important parameters are ion size, coordination, and electro-negativity. Table 2 indicates the variation of the crystal radii of group-VI ions in tetrahedral coordination in comparison with the radius of Mn^{6+} . The Mn^{6+} ion with its crystal radius of 39.5 Å might easily substitute for the larger Mo^{6+} or W^{6+} ions. Nevertheless, no significant doping was found in our molybdates and tungstates. Not even in a chromate, with its Cr^{6+} crystal radius being similar to that of Mn^{6+} , could significant doping be observed [17]. In contrast, BaSO_4 and BaSeO_4 exhibit efficient incorporation. The S^{6+} crystal radius of the former compound is much smaller, whereas the Se^{6+} crystal radius of the latter compound is comparable to that of Mn^{6+} . These observations suggest that the crystal radius of Mn^{6+} is not the crucial parameter that governs its incorporation into a specific host lattice.

Since hexavalent manganese exists exclusively in the form of the MnO_4^{2-} complex ion, the whole manganate tetrahedron incorporates into the crystal structure instead of the XO_4^{2-} tetrahedron. The coordination spheres of the XO_4^{2-} tetrahedron differ in hosts that crystallize in different

Ion	Crystal radius (Å) [24]	Example of the Mn^{6+} -doped material	Space group [26]	Doping level
S^{6+}	26	$\text{BaSO}_4:\text{Mn}^{6+}$	$Pnma$	240–2100 ppm – pink crystals
Mn^{6+}	39.5	(BaMnO_4)	$Pnma$	Dark-green crystals
Cr^{6+}	40	$\text{SrCrO}_4:\text{Mn}^{6+}$	$P2_1/n$	45 ppm – yellow crystals [17]
Se^{6+}	42	$\text{BaSeO}_4:\text{Mn}^{6+}$	$Pnma$	1000 ppm – ink-blue crystals [17]
Mo^{6+}	55	$\text{BaMoO}_4:\text{Mn}^{6+}$	$I4_1/a$	< 60 ppm – light-green crystals
W^{6+}	56	$\text{BaWO}_4:\text{Mn}^{6+}$	$I4_1/a$	< 60 ppm – light-green crystals

TABLE 2 Crystal radii of group-VI ions in tetrahedral oxo-coordination, which may be substituted by the Mn^{6+} ion. Examples of Mn^{6+} -doped materials are given with the indication of their space group, crystal color, and estimated doping level

space groups (see Table 2). All compounds that show efficient incorporation of the MnO_4^{2-} complex ion as well as the stoichiometric BaMnO_4 compound belong to the orthorhombic space group $Pnma$. SrCrO_4 , which incorporates only 45 ppm of Mn^{6+} , crystallizes in the orthorhombic space group $P2_1/n$ with different coordination symmetry of the MnO_4^{2-} complex than in the space group $Pnma$. Finally, molybdates and tungstates crystallize in the tetragonal space group $I4_1/2$, which does not allow for a significant doping level.

We conclude that, for the efficient incorporation of Mn^{6+} , the host crystal structure has to satisfy not only the condition of a hexavalent ion in a tetrahedral oxo-coordination but also the orthorhombic space group $Pnma$ and coordination environment of the XO_4^{2-} tetrahedron. Thus, the observed low incorporation of Mn^{6+} into molybdates and tungstates is not caused by an inapplicability of the flux growth but most probably by the intrinsic crystallographic properties of dopant and host material.

Furthermore, investigation of the manganese distribution in our grown $\text{BaSO}_4:\text{Mn}^{6+}$ crystals revealed that the actual concentration varies with growth time. Figure 4 represents the cross section of a $\text{BaSO}_4:\text{Mn}^{6+}$ crystal in which the actual manganese concentration was measured along the [010] direction using EPMA. The manganese concentration decreases with distance from the nucleus in the geometric center of the crystal due to the reduction of Mn^{6+} with growth time, resulting in decreasing Mn^{6+} concentration in the chloride solution.

Increasing the initial concentration of K_2MnO_4 in the solution from 0.2 to 15 mol% did not lead to any significant increase in Mn^{6+} incorporation. The maximum concentration detected was 2100 ppm. This phenomenon may originate in either a significant acceleration of the reduction of manganese with increasing concentration or a limitation of the maximum possible manganese concentration that can be incorporated into BaSO_4 single crystals. The same phenomenon is probably present and becomes important already at significantly lower manganese concentrations in all the tungstates and molybdates investigated.

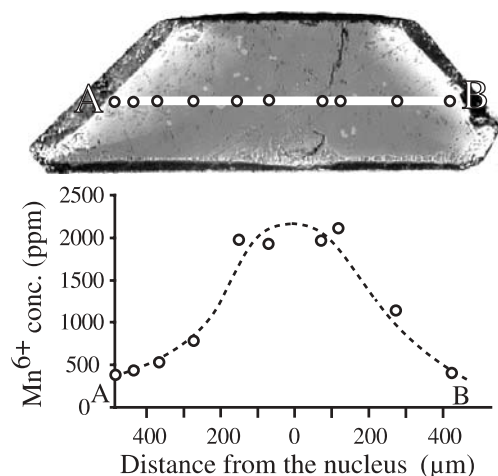


FIGURE 4 Distribution of manganese in a flux-grown $\text{BaSO}_4:\text{Mn}^{6+}$ crystal, measured by EPMA

3.3

Quantitative spectroscopic investigation of $\text{BaSO}_4:\text{Mn}^{6+}$

The Mn^{6+} concentration was too low in our molybdate and tungstate crystals to perform optical absorption measurements. In the following, we concentrate on the quantitative spectroscopy of $\text{BaSO}_4:\text{Mn}^{6+}$.

Polarized absorption measurements were carried out with a Lambda 9 Perkin-Elmer spectrophotometer fitted with a closed-cycle helium cryostat (Scientific Instruments 202) for sample cooling to 10 K. Thin plates of $\text{BaSO}_4:\text{Mn}^{6+}$ with different measured manganese concentrations were polished parallel to the well-developed (101), (011), and (210) crystal faces. Polarized absorption spectra were recorded for all three polarizations. Figure 5a represents the variation of the absorption coefficient parallel to the crystal b axis for different actual Mn^{6+} concentrations at room temperature. As expected, the absorption coefficient increases proportional to the Mn^{6+} concentration. Since the manganese concentrations were determined with good accuracy, correct absorption cross sections could be calculated. Absorption cross sections at 10 K for all three polarizations are shown in Fig. 5b. Their characteristics are similar to the absorption spectra published earlier by Brunold and Güdel [19]. According to that publication, the absorption bands are assigned as ${}^2E \rightarrow {}^2T_2$ between 700 and 900 nm and a ligand-to-metal charge-transfer band between 460 and 600 nm.

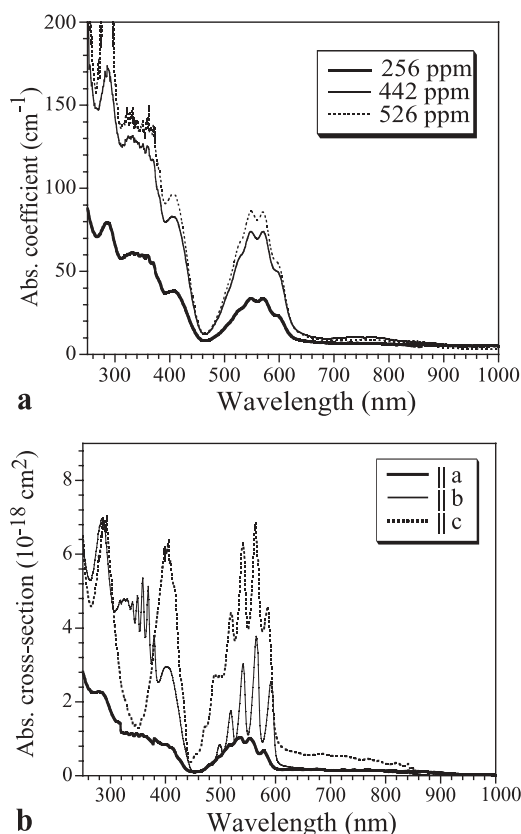


FIGURE 5 Absorption spectra of $\text{BaSO}_4:\text{Mn}^{6+}$ crystals: **a** variation of the absorption coefficient with Mn^{6+} concentration for the polarization $\parallel b$ at room temperature; **b** absorption cross sections for different polarizations at 10 K

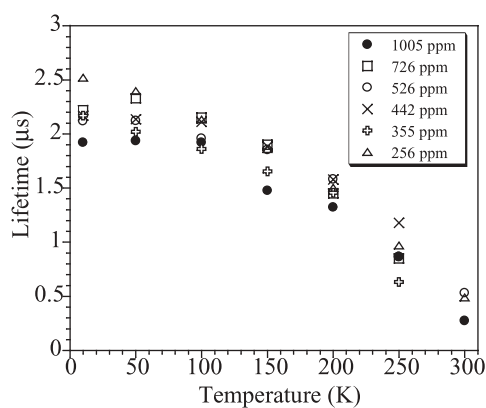


FIGURE 6 Variation of the fluorescence lifetime of $\text{BaSO}_4:\text{Mn}^{6+}$ with temperature for different manganese concentrations

For the fluorescence-lifetime measurements, the samples were excited with a continuous-wave Ar-ion laser operating at 514.5 nm. Pulsed excitation was obtained by passing the beam through an acousto-optic modulator (Newport EOS-AOM) connected to a function generator (HP 3325 A synthesizer). The generated pulses were characterized by a duration of 25 μs and an on/off switch time of 110 ns. Fluorescence-decay curves at 984 nm were measured with a monochromator (Chromex 500 IS) using a RG-850 filter at the entrance slit and detected by a photomultiplier tube (Hamamatsu R5108). The variation of the lifetime with temperature and Mn^{6+} concentration is shown in Fig. 6. The fluorescence lifetime is approximately 2.2 μs at 10 K, but drops to approximately 0.5 μs at room temperature. This behavior is probably due to an increase of non-radiative relaxation with increasing temperature. Assuming a radiative quantum efficiency of 100% at low temperature, the radiative quantum efficiency at room temperature is reduced to roughly 20%. This value is in agreement with an earlier measurement of the relative fluorescence intensity versus temperature [20]. Possible concentration quenching of the fluorescence lifetime at higher Mn^{6+} concentrations has not been observed or lies within the experimental error of our set-up.

4 Conclusions

In this paper, we have investigated the growth of AXO_4 crystals, with $\text{A} = \text{Ca}, \text{Sr}, \text{Ba}$ and $\text{X} = \text{Mo}, \text{W}$ as well as BaSO_4 by the flux method. By use of the ternary NaCl-KCl-CsCl flux as a solvent, growth temperatures could be reduced to 600–475 $^{\circ}\text{C}$, which is considerably lower than in the case of individual chloride solvents or growth from the melt. The growth conditions were optimized with respect to solute concentration and solubility of the AXO_4 compounds. Crack-free, transparent, and colorless crystals were obtained.

The low growth temperatures enabled us to perform a systematic investigation of doping the AXO_4 hosts with Mn^{6+} , which is a promising activator ion for tunable solid-state lasers. The hexavalent oxidation state of manganese in the solution could be partly stabilized by an oxidizing environment. The incorporation of Mn^{6+} is governed by the coordination of the MnO_4^{2-} tetrahedron in the crystal, with the ortho-

rhombic space group $Pnma$ being preferred, and is generally limited to rather low doping levels. For molybdates and tungstates, the doping levels were less than 60 ppm, whereas BaSO_4 incorporated up to 2100 ppm of Mn^{6+} . After determination of the Mn^{6+} concentration and its variation in BaSO_4 , we derived correct absorption cross sections from absorption measurements. The room-temperature luminescence quantum efficiency is approximately 20%. Quenching of the luminescence lifetime at high Mn^{6+} concentrations was found to be insignificant.

In view of the low doping levels of Mn^{6+} that were found in tungstates and molybdates, these active-ion/host combinations do not seem to be suitable as solid-state laser materials. On the other hand, BaSO_4 with its higher capability to incorporate Mn^{6+} and the reasonably long Mn^{6+} upper-state lifetime and relatively high quantum efficiency at room temperature may allow us to demonstrate a novel solid-state laser from this material in the future.

ACKNOWLEDGEMENTS The authors thank K.J. Schenk for the XRD measurements, F. Bussy for the EPMA measurements, and T.C. Brunold, S. Oishi, and S. Kück for fruitful discussions. This work was partially supported by the Swiss National Science Foundation.

REFERENCES

- 1 B.N. Litvin, L.N. Demyanets, L.S. Garashina: in *Growth of Crystals*, Vol. 4 (Consultants Bureau, New York 1963) p. 134
- 2 R.H. Gillette: *Rev. Sci. Instrum.* **21**, 294 (1950)
- 3 L.B. Barbosa, D. Reyes Ardila, C. Cusatis, J.P. Andreeta: *J. Cryst. Growth* **235**, 327 (2002)
- 4 S. Zerfoss, L.R. Johnson, O. Imber: *Phys. Rev.* **75**, 320 (1949)
- 5 J.J. Rubin, R.A. Thomas: *J. Am. Ceram. Soc.* **48**, 100 (1965)
- 6 H. Sawada, Y. Takeuchi: *Z. Kristallogr.* **191**, 161 (1990)
- 7 B.N. Roy: *Crystal Growth from Melts. Applications to Growth of Groups 1 and 2 Crystals* (Wiley, Chichester 1992)
- 8 D.O. Voigt, H. Neels: *Krist. Tech.* **6**, 651 (1971)
- 9 A. Packter, B.N. Roy: *Krist. Tech.* **6**, 39 (1971)
- 10 S. Oishi, Y. Endo, T. Kobayashi, I. Tate: *Nippon Kasagu Kaishi* **9**, 1191 (1979) (in Japanese)
- 11 D. Ehrentauf, M. Pollnau: *J. Cryst. Growth* **234**, 533 (2002)
- 12 T.C. Brunold, H.U. Güdel, S. Kück, G. Huber: *J. Opt. Soc. Am. B* **14**, 2373 (1997)
- 13 D. Ehrentauf, M. Pollnau, S. Kück: *Appl. Phys. B* **75**, 59 (2002)
- 14 M. Pollnau: *J. Luminesc.* **102–103**, 797 (2003)
- 15 M. Pollnau, R.P. Salathé, T. Bhutta, D.P. Shepherd, R.W. Eason: *Opt. Lett.* **26**, 283 (2001)
- 16 A.M. Kowalevich, T. Ko, I. Hartl, J.G. Fujimoto, M. Pollnau, R.P. Salathé: *Opt. Express* **10**, 349 (2002)
- 17 R.P. Schenker, T.C. Brunold, H.U. Güdel: *Inorg. Chem.* **37**, 918 (1998)
- 18 J.S. Booth, D. Dallimore, G.R. Heal: *Thermochim. Acta* **39**, 281 (1980)
- 19 T.C. Brunold, H.U. Güdel: *Inorg. Chem.* **36**, 1946 (1997)
- 20 T.C. Brunold, H.U. Güdel: *Chem. Phys. Lett.* **249**, 77 (1996)
- 21 D.R. Lide (ed.): *CRC Handbook of Chemistry and Physics*, 81st edn. (CRC, Boca Raton, FL 2000)
- 22 E.M. Levin, C.R. Robbins, H.F. McMurdie: *Phase Diagrams for Ceramists*, different edns. (American Ceramic Society, Columbus, OH 1969)
- 23 A. Packter: *Cryst. Res. Technol.* **17**, 377 (1982)
- 24 R.D. Shannon: *Acta Crystallogr. A* **32**, 751 (1976)
- 25 J.-F. Bérar: XND, ver. 1.16, Laboratoire de Cristallographie CNRS, Grenoble
- 26 K.-H. Hellwege, A.M. Hellwege (eds.): *Numerical Data and Functional Relationships in Science and Technology* (Landolt-Börnstein Ser. **III/7**, Part f) (Springer, Berlin 1977)
- 27 S.C. Jain, S.K. Agarwal, G.D. Sothia: *J. Phys. Chem. Solids* **32**, 897 (1971)
- 28 S. Kakigi, T. Harami, A. Okuda: *J. Phys. Soc. Jpn.* **57**, 1111 (1988)
- 29 F.A. Cotton, G. Wilkinson: *Advanced Inorganic Chemistry* (Wiley, New York 1988)